Chinese Chemical Letters 36 (2025) 110129

Contents lists available at ScienceDirect

Chinese Chemical Letters

journal homepage: www.elsevier.com/locate/cclet

Dual-site Se/NC specific peroxidase-like nanozyme for highly sensitive methimazole detection

Yuwan Lu, Xiaodan Zhang, Yuming Huang*

Key Laboratory of Eco-environments in Three Gorges Reservoir Region (Ministry of Education), College of Chemistry and Chemical Engineering, Southwest University, Chongqing 400715, China

ARTICLE INFO

Article history:
Received 27 February 2024
Revised 6 June 2024
Accepted 14 June 2024
Available online 15 June 2024

Keywords:
Se/NC peroxidase-like nanozyme
Dual active sites
Colorimetric assay
Methimazole
Environmental analysis

ABSTRACT

Tuning the nanozyme's activity and specificity is very crucial for developing highly sensitive sensors for various applications. Herein, selenium-doped porous N-doped carbon skeletons (Se/NC) nanozymes with highly specific peroxidase-like activity were synthesized by a MOF-pyrolysis-doping protocol. Se doping adjusted the electronic structure of NC by introducing more vacancies, defective carbon and graphitic N, and endowed the resultant Se/NC enhanced charge transfer and substrate affinity. The Se/NC exhibited specific peroxidase-mimicking activity and could catalyze 3,3′,5,5′-tetramethylbenzidine oxidation by H_2O_2. Density functional theory (DFT) calculations and experimental trials indicated that both Se=O and C–Se–C species were the main active sites of Se/NC. The C–Se–C bond is the main catalytic active site endowing Se/NC with the property of nanozyme, while the Se=O bond effectively enhances its affinity to H_2O_2 and accelerate H_2O_2 dissociation. The Se/NC showed an approximately 185-fold increase in peroxidase-like activity compared to NC. Based on the inhibition of the peroxidase-like activity of Se/NC by methimazole, a colorimetric sensor was developed to achieve its sensitive detection with 2 nmol/L of limit of detection. It was successfully used for detecting methimazole in real samples. Current Se doping strategy simplifies the fabrication process of high performance specific nanozyme and promises great potential for environmental analysis.

Nanozymes are a cross-product of biological enzymes, nanomaterials and surface catalysts [1], which bridge the fields of inorganic nanomaterial and biology. To date, thousands of nanozymes have been designed and developed [2–5] for use in sensing [6–8], catalysis [9], environmental protection [10], antibacterial [11] and tumor therapy [12]. Among them, the transition metal- and precious metal-based nanozymes attracted large interest credited to their high catalytic efficiency [13–17]. However, the metal-based nanozymes, in particular, the noble metal-based ones have some drawbacks, *i.e.*, high cost, low selectivity, poor durability and potential metal toxicity. Constructing metal-free nanozymes with high activity, stability and low cost is more attractive to realize their potential practical use. Relative to the metal-based nanozymes, the metal-free carbon-based nanozymes promise practical merits, such as low cost due to their earth abundance, good electrical conductivity, high surface area, rich active sites, higher chemical stability and less biological toxicity [18,19]. However, relative to that of the metal-based ones, the catalytic performance of the carbon-based nanozymes is limited. Several strategies, like morphology regulation, surface functionalization and heteroatom-doping, were used to improve their catalytic activity [19,20]. Particularly, the heteroatoms (*e.g.*, N, P, S, B) doping of non-metal-based carbon received increasing attention because single doping or co-doping can tune the charge redistribution among carbon atoms and introduce additional active sites *via* increasing carrier density and electrical conductivity of carbon, or synergistic effect [21,22], finally boosting their enzyme-like activities.

Although the heteroatom-doping strategy has made some progress, it still has shown promising research prospects due to the extensive range of heteroatom-derived precursors and the structural diversity of carbon-based nanozymes. Selenium (Se) is a non-metallic chalcogen element with a large atom size (atomic radius = 103 pm), high polarizability and rich d-electron. It can enhance the electrical transport properties of carbon skeletons [23]. Se, with resembling atomic electronegativity (EN = 2.55) to carbon element, is one kind of doping heteroatom for carbon-based materials and has received interest in several fields [24]. In addition, Se is also the active center of various antioxidant enzymes, including glutathione peroxidase and thioredoxin reductase [24]. Thus, Se-doping is likely a promising strategy to construct

* Corresponding author.
E-mail address: ymhuang@swu.edu.cn (Y. Huang).

https://doi.org/10.1016/j.cclet.2024.110129
1001-8417/

high performance nanozyme. However, rare attention is paid on the exploration of Se-doped non-metallic nanozyme [25].

Metal-organic frameworks (MOFs) containing orderly metal sites and organic ligands are one of good templates or self-sacrificial precursors for developing carbon composites *via* high-temperature annealing in an inert atmosphere [26]. The MOFs derived N-doped carbon skeletons not only have a controllable pore structure to facilitate the catalytic mass transfer process but also supply accessible anchor sites (*i.e.*, pores and N sites) for the incorporation of heterogeneous elements [10,26]. Thus, it is a controllable strategy to synthesize co-doped carbon skeletons for promising applications. For instance, Zn evaporation in the ZIF-8 during high-temperature treatment leaves the N-doped carbon skeleton with high specific surface area. This can be used to anchor Bi nanoparticles (NPs) for lithium-ion battery [27].

Herein, for the first time, we reported the development of the Se, N-codoped porous carbon skeleton (Se/NC) nanozymes *via* a MOF-pyrolysis-doping strategy. SeO_2 was chosen as Se source because it has lower cost, less toxic and more stable than Se powder or Na_2SeO_3 [28]. In addition, adsorption of SeO_2 onto carbon materials is thermodynamically more favorable than that of Se(0) [29], which is beneficial to enhance the doping amount of selenium to create more active sites. The Se/NC exhibits specific peroxidase (POD)-mimicking activity and no oxidase (OXD)-mimicking activity. Relative to that of NC, the POD-like activity of Se/NC nanozyme increased by nearly 185-fold. Theoretical and experimental trials indicated that both Se=O and C–Se–C species were the main active sites of Se/NC, and the former was highly related to its affinity to H_2O_2. The catalytic mechanism exploration suggested that the C–Se–C bond is the main catalytic active site endowing Se/NC with the property of nanozyme, while the Se=O bond effectively enhances the specificity and activity of the Se/NC nanozyme by promoting its affinity to H_2O_2 and accelerating H_2O_2 dissociation. The catalytic mechanism investigation revealed that the Se/NC nanozymes can promote the decomposition of H_2O_2 to produce $^{\bullet}OH$ and $^1O_2$. In addition, the introduction of methimazole (MMI) inhibited the POD-like activity of Se/NC. Based on this, a facile and sensitive colorimetric assay was developed to determine MMI with low limit of detection (LOD) (2 nmol/L). MMI is selected as target because it belongs to thionamide antithyroid drug, which is widely used for the treatment of hyperthyroidism [30]. The World Health Organization's International Agency for Research on Cancer catalogued MMI as a group 3 carcinogen. Thus, its sensitive and selective determination is of significance. Various methods have been developed to determine MMI, including HPLC [31], mass spectrometry [32], fluorometry [33], electrochemistry [34], and surface-enhanced Raman spectroscopy (SERS) [35,36]. Among various assays, the colorimetric ones hold the merits of convenient operation, fast response, and low instrument cost [37]. In particular, the nanozyme-based colorimetric sensing systems have drawn enormous attention [38]. Constructing a sensitive and effective sensing platform for colorimetric detection of MMI is in favor of further expanding the application prospect of nanozymes. However, to our knowledge, no nanozyme-based colorimetric method has been developed for the detection of MMI.

Fig. 1a depicts the schematic of the preparation of the Se/NC skeleton *via* a MOF-pyrolysis-doping protocol (see synthetic details in Supporting information). First, *via* a co-precipitation reaction of Zn^{2+} ions with 2-methylimidazole, the uniform dodecahedron ZIF-8 precursor with diameters of 200–300 nm was prepared (Fig. S1a in Supporting information). Its X-ray diffraction (XRD) pattern (Fig. S1b in Supporting information) can be well indexed to simulation [39]. After pyrolysis at 900 °C for 3 h under the Ar atmosphere, the ZIF-8 was transformed to the N-rich carbon matrix, *i.e.*, NC. The pyrolysis of the mixture NC and SeO_2 powder at 500 °C under Ar produced the Se/NC. Both the NC and Se/NC displayed the dodecahedron nanostructure (Figs. S2a and b in Supporting information) and similar XRD patterns (Fig. S2c in Supporting information). In the XRD, the main peaks at 2θ of 26.6° and 44.7° are attributed to the (002) and (100) planes of graphitic carbon (PDF #25-0284) [40], and no SeO_2 peaks are detected. From the transmission electron microscopy (TEM) images (Figs. 1b and c), there are only dodecahedron morphology carbon nanoframes without discernible Zn or ZnSe NPs in the Se/NC. The high-resolution TEM (HRTEM) image shows no obvious crystal lattices (Fig. 1d). The element mapping images and energy dispersive X-ray spectrum (EDX) (Fig. 1e and Fig. S3 in Supporting information) indicate that the C, N, and Se species are homogeneously distributed in the Se/NC. The Se contents are ~5.08 wt% and 7.59 wt% based on EDX and inductively coupled plasma optical emission spectroscopy, respectively. Fig. S4 (Supporting information) shows the X-ray photoelectron spectroscopy (XPS) survey spectra of NC and Se/NC. As shown, in comparison with that of NC, the XPS of Se/NC has a new characteristic peak of Se 3d orbit, consistent with the EDX result (Fig. S3). This implies that the Se has been successfully doped into the NC. The high-resolution C 1s spectrum in Fig. 2a exhibits four peaks, associated with sp^2–C (284.6 eV), sp^3–C (285.3 eV), C–N/C–Se (286.3 eV), and C=O (288.6 eV) [41], respectively. Since the binding energies of C–N and C–Se are close, it is difficult to distinguish them [42]. The spectrum of N 1s showed four peaks at around 398.5 eV, 400.1 eV, 401.1 eV and 402.3 eV (Fig. 2b). They are attributed to pyridinic N, pyrrolic N, graphitic N, and oxidized N [43], respectively. As show in Table S1 (Supporting information), relative to those in the NC, the amount of sp^2–C species are obviously reduced and those of sp^3–C and C–N/C–Se species are increased slightly in the Se/NC. This indicates that the incorporation of Se increases the defect degree of the resultant Se/NC, which are considered as active sites to promote electron transfer and increase the catalytic activity [44]. In addition, the graphitic N content in the Se/NC (28.83%) is significantly higher than that of NC (18.70%). The graphitic N is not only the adsorption site of H_2O_2 [45], but also plays key role in the activation of O–O band to produce singlet oxygen ($^1O_2$) [46]. High-resolution Se 3d XPS spectra (Fig. 2c) can be further deconvolved into two peaks at binding energies of 58.9 eV (Se=O) and 56.3 eV (C–Se–C) [47]. There is no Se^{2-} (54.5–55.3 eV) in the Se/NC [48].

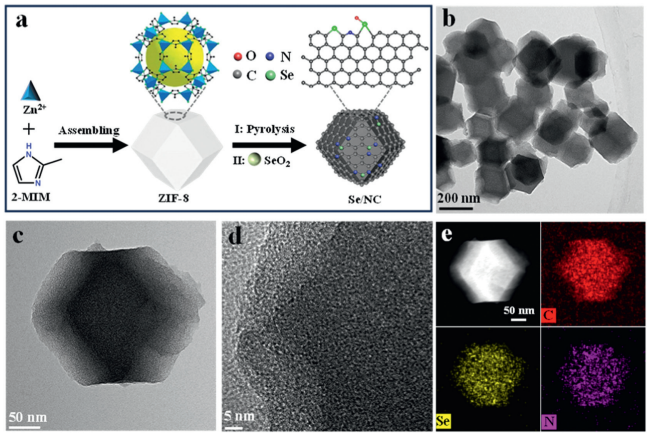

Fig. 1. (a) Schematic of the synthesis of Se/NC. (b) TEM image, (c) enlarged TEM image, and (d) HRTEM image of Se/NC. (e) HAADF-STEM and corresponding elemental mapping of Se/NC.

Raman spectra show two obvious peaks at 1332 and 1586 cm^{-1} (Fig. S5 in Supporting information), ascribing to the D band (disorder structure) and G band (graphitic structure) [40], respectively. The calcination temperature has almost no effect on the ratio of D band intensity to G band intensity (I_D/I_G) in the range of 350–600 °C (Fig. S5a), while the I_D/I_G value increases with the

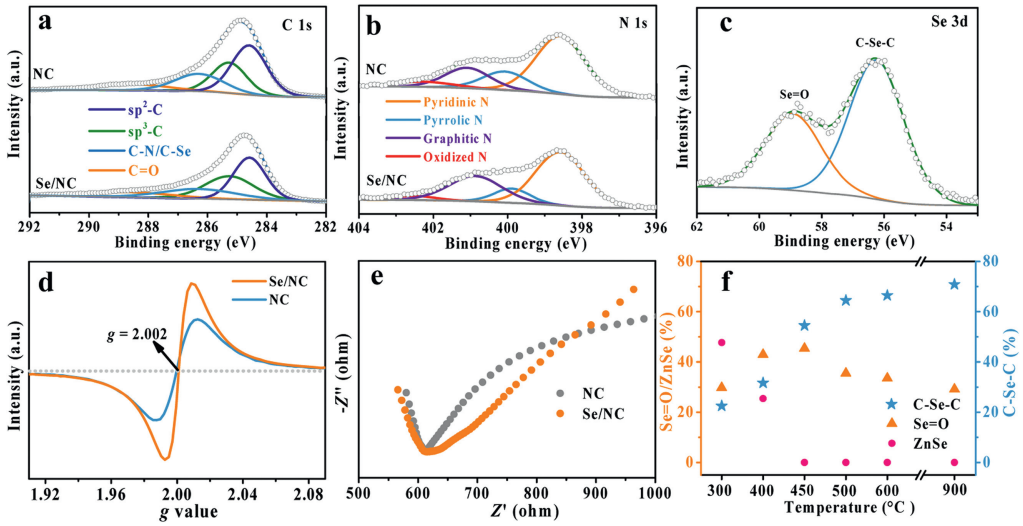

Fig. 2. High-resolution (a) C 1s and (b) N 1s XPS spectra of NC and Se/NC. (c) Se 3d XPS spectrum of Se/NC (500 °C). (d) Solid EPR spectra and (e) EIS of the as-prepared NC and Se/NC. (f) Contents of Se species at temperatures of 300–900 °C based on Se 3d XPS results.

proportion of Se (Fig. S5b). The I_D/I_G for Se/NC was 1.06, which was higher than that of 0.99 for NC (Fig. S5b). This indicates the abundant defects in the Se/NC. The higher D peak is also representative of more defects induced by the selenylative etching, such as vacancies or substitutional Se atoms in the carbon nanostructure. Solid electron paramagnetic resonance (EPR) spectra (Fig. 2d) show an asymmetric signal peak centered at $g = 2.002$ in both NC and Se/NC, which is ascribed to the broken bonds at the defect sites [49,50]. Obviously, the Se/NC displays higher asymmetric signal peak than the NC, indicating the formation of more defects in the Se/NC.

The electrochemical impedance spectroscopy (EIS) result shows small half-circle radius of the Se/NC relative to that of NC (Fig. 2e). This implies that the Se/NC has faster charge transfer ability than NC [51]. The N_2 adsorption-desorption isotherms display type I for the ZIF-8, NC and Se/NC samples (Fig. S6a in Supporting information), indicating their microporous nature. The Brunauer-Emmett-Teller (BET) specific surface area and pore volume are 800.08 m^2/g and 0.52 cm^3/g, and 759.32 m^2/g and 0.49 cm^3/g for the NC and Se/NC (Fig. S6b and Table S2 in Supporting information), respectively. Thermogravimetric analysis (TGA) was carried out in a nitrogen atmosphere (30–1100 °C) to investigate the reaction between SeO_2 and NC. As depicted in Fig. S7 (Supporting information), the TGA curve shows a mass decrease from 30 °C to 200 °C, corresponding to the absorbed water molecules loss. As the calcination temperature was further increased, the TGA curve started to steepen, indicating that SeO_2 (sublimation point: 315 °C) was evaporated at high-temperature and reduced to ZnSe by NC [47]. High-resolution Se 3d XPS spectra of SeO_2 powder and Se/NC obtained at different temperatures are shown in Figs. S8a–f (Supporting information). As displayed in Fig. S8a, SeO_2 powder showed typical Se=O specie at 59.0 eV without other peaks [52]. In the 300–400 °C range, the deconvoluted Se 3d spectra showed three major peaks at 58.8 eV, 56.3 eV and 55.3 eV (Figs. S8b and c), corresponding to Se=O, C–Se–C and ZnSe, respectively. This suggests the formation of different Se species on the NC framework. At temperature ≥ 450 °C, the ZnSe disappeared and major Se species are Se=O and C–Se–C in the Se/NC (Fig. 2c, Fig. S8d–f). Fig. 2f shows the dependence of various Se species on the carbonation temperature based on Se 3d XPS analysis. Obviously, the Se=O species gradually decreased, while the C–Se–C species increased at temperature above 450 °C. Based on these observations, after the introduction of Se, the physicochemical property of the NC framework was completely changed and may display excellent catalytic activity.

The POD-mimicking activity of Se/NC was evaluated in the catalytic oxidation of substrates 3,3′,5,5′-tetramethylbenzidine (TMB) (see detailed procedure in Supporting information). From Fig. 3a, only the Se/NC was capable of significantly catalyzing TMB oxidation by H_2O_2 to generate blue oxTMB (inset in Fig. 3a), exhibiting a strong distinctive absorbance peak at 652 nm (A_{652}), and negligible color change occurred without the H_2O_2. Meanwhile, the other control groups had no obvious absorption at 652 nm. A similar results were observed with other substrates, *i.e.*, *o*-phenylenediamine (OPD) and 2,2′-azino-bis(3-ethylbenzothiazoline-6-sulfonic acid) diammonium salt (ABTS) (Fig. S9 in Supporting information), implying that the Se/NC displayed prominent POD-like activity and inappreciable OXD-like activity. From the kinetic curve in Fig. 3b, only the Se/NC + TMB + H_2O_2 system exhibits obvious A_{652} variance.

Since the amount of SeO_2 and the pyrolysis temperature during the synthesis process may affect the POD-like activity of Se/NC nanozyme, these two parameters were optimized. As shown in Figs. S10a and b (Supporting information), the optimal synthesis conditions were as follows: Mass ratio of SeO_2 to NC of 1:1 and calcination temperature of 500 °C. The effects of Se/NC dosage, solution pH, reaction time, and reaction temperature on the catalytic activities of Se/NC were explored. Fig. S11 (Supporting information) shows the changes in the POD-like activity of the Se/NC nanozyme at different reaction times (0–32 min, Fig. S11a), Se/NC dosages (2.5–30 mg/L, Fig. S11b), reaction temperatures (10–50 °C, Fig. S11c), and solution pH (2.5–5.0, Fig. S11d). Finally, 10 mg/L of Se/NC, pH 3.5, 25 °C, and 20 min reaction time were chosen.

Under these conditions, the specific activity (SA, U/mg) of Se/NC was evaluated based on Jiao *et al.* [53]. The slopes of the initial linear portion of the reaction curve for Se/NC at different concentrations were determined and plotted with the corresponding mass to calculate the SA value (Eqs. S1 and S2 in Supporting information, Fig. 3c). From Fig. 3d, the SA value of the Se/NC nanozyme is 0.26 U/mg, while it is only 0.0014 U/mg for the NC nanozyme (Fig. S12a in Supporting information). Obviously, Se doping led to about 185-fold increase in peroxidase-like activity of NC nanozyme. Although it is lower than that of metal-based peroxidase nanozymes, such as CeO_2 [54], Pt/CeO_2-650R [55], MnO_2 NPs [56], CoAl-LDHs [57], f-MnNC [58], f-CuNC [58], and f-FeNC [58], it is very close to that of NiFe-LDHs and FeAl-LDHs [57]. Also,

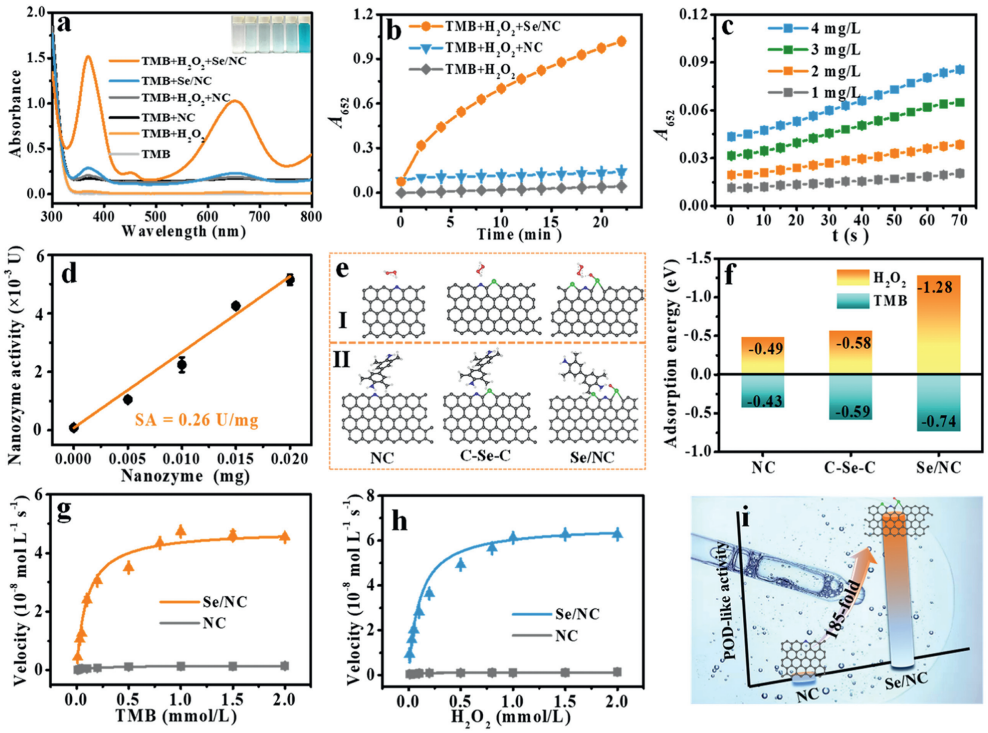

Fig. 3. The peroxidase-like activity of Se/NC. (a) Typical absorption spectra of TMB colorimetric reaction (300–800 nm) with different samples (inset: photos of each group). (b) Absorbance-time curves of TMB chromogenic reaction catalyzed by H_2O_2, H_2O_2 + NC, and H_2O_2 + Se/NC, respectively. (c) Initial linear portion of reaction–time curves for Se/NC nanozyme with different concentrations. (d) The specific activities (U/mg) of Se/NC nanozymes. (e) Optimized adsorption configurations of (I) H_2O_2 and (II) TMB on the NC site, C–Se–C site and Se/NC (C–Se–C & Se=O site) and (f) the corresponding adsorption energy values. (g, h) Michaelis-Menten curves for Se/NC and NC. (i) Comparison of the POD-like activity of Se/NC with NC.

it is higher than that of Fe_3O_4 [59], chitosan-Fe_3O_4 [60], Cu_1/CeO_2 [61], V_2O_5 [62], $Au_{24}Ag_1$ clusterzymes [63], CDs/LDHzyme [64], E-Kaol/MFO-250 [65], NiAl-LDHs [57], Cu-CDs-300 [66], f-ZnNC and f-CoNC [58], see Table S3 in Supporting information for details.

The relative standard deviation (RSD) of the catalytic activity variation of the Se/NC among five batches is 4.95%, indicating that the variation between different batches is negligible (Fig. S13a in Supporting information). This implies that the synthesis of the Se/NC mimic enzyme is reproducible. Moreover, the Se/NC nanozyme exhibits a high storage stability, and no distinct activity decrease was observed after 90 days of storage in an aqueous solution and preservation at room temperature (Fig. S13b in Supporting information). In addition, Fig. S13c (Supporting information) shows that the Se/NC exhibits good temperature (4–75 °C) and pH (2–12) resistance.

From Fig. 2f, when the calcination temperature reached 450 °C, the content of the Se=O bond reaches the highest (45.43%), but Se/NC nanozyme obtained at 500 °C possessed the highest activity. In the Se/NC nanozyme obtained at 500 °C, the contents of Se=O and C–Se–C were 35.45% and 64.55%, respectively. This indicates that both Se=O and C–Se–C species controlled the POD-like activity of Se/NC. The content of C–Se–C species increased slowly at the calcination temperature from 450 °C to 900 °C, but that of Se=O decreased obviously when the calcination temperature was above 450 °C. Hence, both Se=O and C–Se–C species were the main active sites, and the content of Se=O was closely related to the affinity of the nanozyme for H_2O_2. To confirm this hypothesis, the density functional theory (DFT) calculations were carried out to simulate the catalytic mechanism of Se/NC. Based on XPS observation, N-doped carbon structure containing C–Se–C and Se=O bonds was chosen to construct the model of Se/NC. Taking into account the crucial roles of C–Se–C and Se=O species, the comparison models were constructed by removing only Se=O bond and both C–Se–C and Se=O bonds, denoted as C–Se–C site and NC site. First, as displayed in Fig. S14 (Supporting information), the charge quantity (Q) of the dual-sites (C–Se–C & Se=O site, Se/NC site) is −0.69 e, which is significantly smaller than those of the NC site (−0.27 e) and C–Se–C site (−0.46 e). This implies that the dual-sites have better catalytic activity with high electron transfer efficiency than single-site. Second, the adsorption model and adsorption energy of TMB and H_2O_2 on different active sites (NC site, C–Se–C site, C–Se–C & Se=O site) were shown in Figs. 3e and f. The adsorption energy of H_2O_2 on the NC site (−0.49 eV) was close to that of H_2O_2 on the C–Se–C site (−0.58 eV), while it was −1.28 eV on the Se/NC, which was much lower than that of the NC site and the C–Se–C site. This indicates that the high affinity of Se/NC nanozyme for H_2O_2 is mainly dependent on the Se=O bond. The DFT results are in agreement with the steady-state kinetics trials. In addition, the introduction of the Se=O bond also increased the adsorption energy of TMB (−0.74 eV), which was conducive to the adsorption of more TMB on the surface of Se/NC nanozyme, further facilitating TMB oxidation. Also, we prepared the Se/NC nanozyme at 900 °C, denoted Se/NC-900. As shown in Fig. S15a (Supporting information), the dodecahedron morphology was preserved perfectly, and only graphite carbon peak appeared in the XRD pattern (Fig. S15b in Supporting information). The specific surface area and pore volume of Se/NC-900 were 1118.13 m^2/g and 0.70 cm^3/g (Figs. S15c and d in Supporting information), higher than those of Se/NC-500 (Table S2 in Supporting information). However, the Se/NC-900 has similar macroscopic properties to Se/NC. For the synthesis of Se/NC-900, the optimal mass ratio of NC to SeO_2 was also 1:1 (Fig. S15e in Supporting information). As shown in Fig. S15f (Supporting information), the reproducibility among independent five-batch preparation of Se/NC-900 is satisfactory, with the RSD of 1.87%. From Fig. S12b (Supporting information), the SA of the Se/NC-900 as POD-like nanozyme is 0.12 U/mg. To quantitatively evaluate the

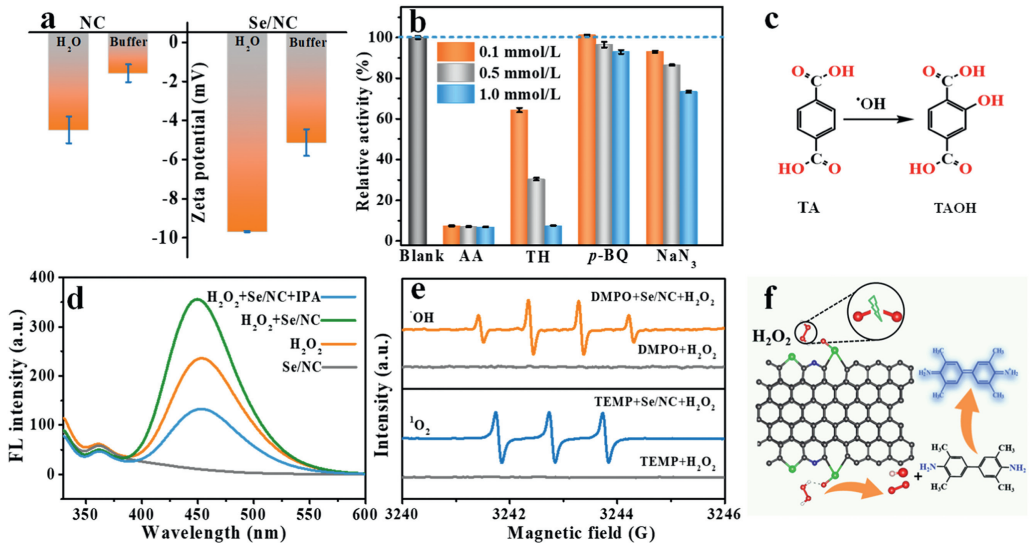

Fig. 4. (a) Zeta potentials of NC and Se/NC suspension in different mediums. (b) The POD-like activity of Se/NC under different quenching agents: the A_{652} of the Se/NC + TMB + H_2O_2 colorimetric system with and without ROS scavengers (AA: scavenging $O_2^{\bullet-}$ and ·OH, TH: scavenging ·OH, NaN_3: scavenging $^1O_2$, *p*-BQ: scavenging $O_2^{\bullet-}$). (c) The equation for the oxidation of TA by ·OH to fluorescent TAOH. (d) Fluorescent emission spectra of TAOH after being exposed to various treatments. (e) EPR spectra showing the ·OH and $^1O_2$ generation. (f) Schematic illustration of the POD-like catalytic process of Se/NC nanozymes.

enzymatic performance, the steady-state kinetics of the NC, Se/NC (Figs. 3g and h, Fig. S16 in Supporting information), and Se-NC-900 (Figs. S17a–d in Supporting information) were investigated *via* a single fitting Michaelis-Menten kinetics under the above optimal conditions [10]. As summarized in Table S4 (Supporting information), for the Se/NC-500, the maximal reaction velocity (V_{max}) and Michaelis-Menten constant (K_m) with TMB were 4.78×10^{-8} mol L^{-1} s^{-1} and 0.099 mmol/L, and the V_{max} and K_m with H_2O_2 were 6.68×10^{-8} mol L^{-1} s^{-1} and 0.107 mmol/L. Obviously, the Se/NC shows a lower K_m value and 29.8-fold higher catalytic velocity than NC for TMB, proving that the Se/NC owns an excellent catalytic performance after Se doping. Besides, the K_m value of Se/NC with H_2O_2 as the substrate is 33.6-fold lower than natural HRP [67] and about half of Se/NC-900, suggesting its distinguished affinity towards H_2O_2. Also, the V_{max} of Se/NC nanozyme was obtained *via* a double fitting method [68]. As shown in Fig. S18 (Supporting information), relative to the traditional single fitting method, the double fitting one gives higher V_{max} values for TMB and H_2O_2. This is likely because, besides substrate concentration, the mass concentration of nanozymes may also influence V_{max} [10] because it depends on the number of catalytic sites. In this work, the conditions of the catalytic kinetics trials for the NC, Se/NC-500 and Se/NC-900 (such as catalyst dosage and each TMB or H_2O_2 concentration) were kept consistent to get comparable kinetic parameters (Table S4). The contents of Se=O and C–Se–C species in the Se/NC-900 were 29.17% and 70.83%, respectively (Fig. 2f). Relative to that in the Se/NC-500 (35.45%), the content of the Se=O bond in the Se/NC-900 was significantly reduced. Also, the Se/NC-900 exhibited nearly 1-fold higher K_m value for H_2O_2 than the Se/NC-500, indicating that the Se=O bond had significantly affected the affinity of Se/NC for H_2O_2. Compared with reported metal-free nanozymes (Table S4), the K_m and V_{max} values of the Se/NC nanozyme were comparable and even better. What's more, compared with NC, the POD-like activity of Se/NC nanozyme increased by about 185-fold (Fig. 3i).

In a word, Se doping adjusted the electronic structure of NC by introducing more vacancies, defective carbon and graphitic N (XPS result), and reduced the mass transfer resistance. Also, the successful Se doping introduced new active sites (like Se=O and C–Se–C species), which simultaneously improved the affinity to H_2O_2 and catalytic capacity of the NC. Finally, Se doping endows more negatively charged surface of Se/NC nanozyme. All above merits eventually led to the high specificity and high activity of peroxidase-like Se/NC nanozymes.

To further investigated the high POD-like catalytic mechanism of nanozymes, the zeta potentials of NC and Se/NC suspension in the water and HAc-NaAc buffer (0.2 mol/L, pH 3.5) medium were measured. As illustrated in Fig. 4a, in comparison with NC, the surface of Se/NC has more negative charges both in the water and buffer. For positively charged TMB, the negatively charged nanozyme enhanced the affinity between the substrate and nanozyme [69].

In general, some reactive oxygen species (ROS), such as $O_2^{\bullet-}$, ·OH, and $^1O_2$ could play crucial roles in nanozyme catalytic reactions. To examine the generation of ROS, the ascorbic acid (AA), thiourea (TH), *p*-benzoquinone (*p*-BQ), and NaN_3 were utilized used as scavengers for ·OH and $O_2^{\bullet-}$, ·OH, $O_2^{\bullet-}$, and $^1O_2$ [13], respectively. As displayed in Fig. 4b, in the Se/NC + TMB + H_2O_2 system, both ·OH and $^1O_2$ play an important role. Further, we investigated the fluorescent probe terephthalic acid (TA) with ·OH to generate a highly fluorescent 2-hydroxyterephthalic acid (TAOH, fluorescent emission peak at 450 nm) molecule to prove that Se/NC nanozyme can decompose H_2O_2 to produce ·OH (Fig. 4c). Compared with TA + Se/NC system, an obvious fluorescence (FL) emission peak appeared at 450 nm after adding H_2O_2. Moreover, the peak intensity decreased after the addition of isopropanol (IPA, scavengers for ·OH), which proved the existence of ·OH again (Fig. 4d). The generation of ·OH and $^1O_2$ was verified by EPR test. As shown in Fig. 4e, the characteristic signals with strength ratios of 1:2:2:1 by using 5,5-dimethyl-1-pyrroline-*N*-oxide (DMPO) as ·OH trapping agent suggested the formation of ·OH, indicating that the Se/NC could catalyze H_2O_2 to generate ·OH [38]. Moreover, the characteristic signals with strength ratios of 1:1:1 by using TEMP (2,2,6,6-tetramethylpiperidine) as $^1O_2$ trapping agent offered credible evidence for the formation of $^1O_2$ [38]. Based on the above outcomes, the process of ·OH and $^1O_2$ generation from H_2O_2 by Se/NC nanozymes is shown in Fig. 4f.

To understand the generation of ·OH and $^1O_2$ theoretically, the Gibbs free-energy profiles for the C–Se–C and Se/NC were explored. As shown in Figs. 5a and b, the intrinsic rate-determining step

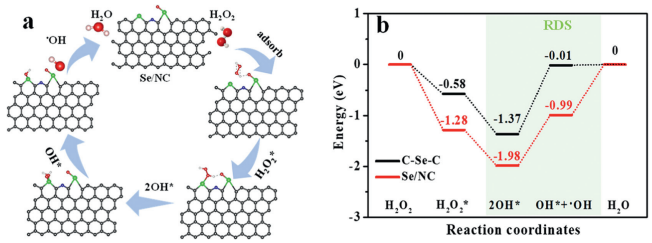

Fig. 5. (a) Proposed reaction route of H_2O_2 reduction on the Se/NC. (b) Energy diagram of the calculated models for the production of ·OH.

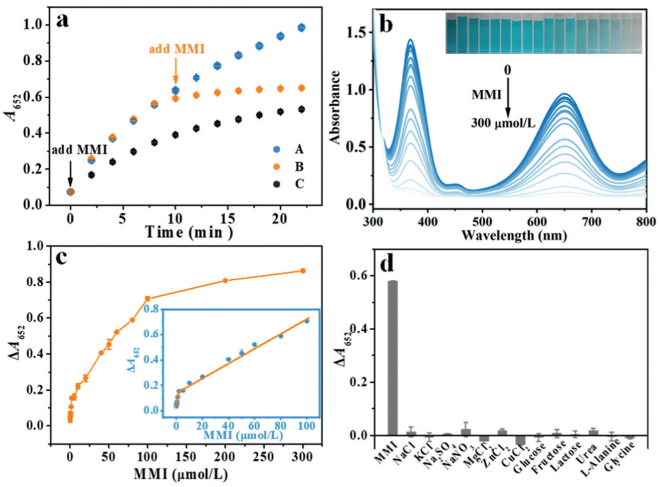

Fig. 6. (a) Kinetic curves of Se/NC-catalyzed TMB oxidation by H_2O_2 in the absence and presence of MMI. (b) The UV–vis absorption curves of Se/NC + TMB + H_2O_2 system with different concentrations of MMI. Insets: corresponding digital pictures. (c) Plots of ΔA_{652} *versus* MMI concentration. Inset is linear plot for MMI detection. (d) Comparison of the ΔA_{652} of the Se/NC catalyzed TMB oxidation by H_2O_2 in the presence of 80 μmol/L MMI or 2 mmol/L other interfering species. Data were presented as mean ± standard deviation ($n = 3$).

(RDS) for both the C–Se–C and Se/NC was the regeneration step of OH* and ·OH from OH*. The former had 1.36 eV energy barrier. However, a much lower barrier of 0.99 eV for Se/NC was obtained. This further indicated the significant energy merits obtained by the introduction of Se=O bond in the Se/NC to generate ·OH. Since Se/NC can activate H_2O_2 to produce both ·OH and $^1O_2$ (Fig. 4e), the energy change of the $^1O_2$ generation path on C–Se–C and Se/NC models was also calculated (Fig. S19 in Supporting information). The results showed that the two models have an identical effect on $^1O_2$ generation. Hence, the Se=O bond in Se/NC acts as the H_2O_2 adsorption site, and the C–Se–C bond acts as the catalytic active site to enhance the POD-mimicking activity of Se/NC. In addition, relative to that in NC, significantly higher graphite N content in the Se/NC can accelerate the electron transfer between the Se/NC and TMB, which is evidenced by the small half-circle radius of the Se/NC in Fig. 2e. This can promote the decomposition of H_2O_2, and thus enhance the POD-like activity [70] of Se/NC.

In terms of the unique POD-mimicking activity of Se/NC without the interference of O_2, we employed Se/NC to detect MMI with the sensing mechanism illustrated in Fig. 6a. As the plots A and B show, the addition of MMI at 10 min obviously led decline in the A_{652} of Se/NC + TMB + H_2O_2 system, implying the reduction of oxTMB by MMI. Moreover, when introduced MMI at the beginning of the reaction (curve C), TMB oxidation was postponed. This is because MMI is a mercapto compound, and the reductive –SH group in the MMI can suppress TMB oxidation *via* consumption of ROS [26] in the Se/NC + TMB + H_2O_2 system. Above outcomes suggest the consumption of ROS by MMI, leading to inhibition of TMB oxidation. The consumption of ROS by MMI was further confirmed by the fluorescent probe TA trial. As shown in Fig. S20 (Supporting information), the FL peak intensity at 450 nm declined with increase in the MMI concentration, indicating that the ·OH was consumed by MMI. In this case, MMI with the concentrations of 0.002, 0.005, 0.02, 0.1, 0.2, 0.5, 1, 2, 5, 10, 20, 40, 50, 60, 80, 100, 200, and 300 μmol/L was successively pre-incubated with Se/NC + TMB + H_2O_2 system to explore the colorimetric analytical performance. From Fig. 6b, the blue color gradually shallowed with an increase in MMI concentration. A good linear relationship between ΔA_{652} (ΔA_{652} is the A_{652} difference without and with MMI) and MMI concentration was established in the ranges of 0.002 −2 μmol/L and 2−100 μmol/L. The linear regression equations were $\Delta A_{652} = 0.061$ [MMI] (μmol/L) + 0.042, $R^2 = 0.9783$ ($n = 8$) and $\Delta A_{652} = 0.0057$ [MMI] (μmol/L) + 0.164, $R^2 = 0.9816$ ($n = 9$) (Fig. 6c), respectively. The LOD for the detection of MMI was 2 nmol/L. Compared to previous reports (Table S5 in Supporting information), the developed colorimetric method shows lower detection limit and broader linear range. As shown in Fig. 6d, MMI could effectively reduce the oxTMB along with the significant change in absorbance at 652 nm. While the values of the ΔA_{652} have inappreciable changes for other interferences, demonstrating the high selectivity for detecting MMI. Moreover, to explore its potential use in actual samples, water sample trials were performed *via* the recovery tests in which the spiked water samples with different levels of MMI (1, 10 and 50 μmol/L) were used (see detailed procedure in Supporting information). As shown in Table S6 (Supporting information), the recoveries of MMI in two water samples were within the range of 97.17%–104.79%, yielding RSD of less than 4.68%, showing high applicability and reliability.

In conclusion, *via* a simple Se doping strategy, we successfully developed specific and highly active peroxidase-like Se/NC nanozymes. The bi-functional property of the Se/NC including the catalytically active sites of C–Se–C and the affinity sites of Se=O greatly promotes electron transfer efficiency and TMB adsorption. Theoretical and experimental trials supported that the C–Se–C species were catalytically active sites of Se/NC, while the Se=O species were highly related to its affinity to H_2O_2. Upon the introduction of H_2O_2, it was efficiently trapped by the Se=O sites, then catalytically decomposed by C–Se–C sites to generate ·OH and $^1O_2$, finally boosting color reaction between Se/NC nanozyme and TMB. The Se/NC nanozyme exhibits specificity POD-like activity without OXD-mimicking activity. Compared with NC, the POD-like activity of Se/NC nanozyme increased nearly by 185-fold. In terms of the quenching effect of methimazole on the Se/NC + TMB + H_2O_2 color reaction system, a selective and sensitive colorimetric assay was developed and successfully used for detecting methimazole in water samples. Our results unveiled a new strategy to tune the activity and specificity of nanozymes *via* introducing dual sites, which may open up new avenue for developing high performance nanozymes for analytical applications.

Declaration of competing interest

The authors declare that they have no known competing financial interests or personal relationships that could have appeared to influence the work reported in this paper.

CRediT authorship contribution statement

Yuwan Lu: Writing – original draft, Methodology, Investigation. **Xiaodan Zhang:** Writing – review & editing. **Yuming Huang:** Writing – review & editing, Supervision, Methodology, Conceptualization.

Supplementary materials

Supplementary material associated with this article can be found, in the online version, at doi:10.1016/j.cclet.2024.110129.

References

[1] W. Yang, X. Yang, L. Zhu, et al., Coord. Chem. Rev. 448 (2021) 214170.
[2] X. Cao, C. Zhu, Q. Hong, et al., Angew. Chem. Int. Ed. 62 (2023) e202302463.
[3] S. Cao, Z. Zhao, Y. Zheng, et al., Adv. Mater. 34 (2022) 2200255.
[4] Q. Zhou, H. Yang, X. Chen, et al., Angew. Chem. Int. Ed. 61 (2022) e202112453.
[5] Y. Wei, J. Wu, Y. Wu, et al., Adv. Mater. 34 (2022) 2201736.
[6] Y. Ai, Z. Hu, X. Liang, et al., Adv. Funct. Mater. 32 (2022) 211043.
[7] Q. Hong, H. Yang, Y. Fang, et al., Nat. Commun. 14 (2023) 2780.
[8] C. Zhu, Q. Hong, K. Wang, et al., Chin. Chem. Lett. 35 (2024) 109560.
[9] X. Lu, S. Gao, Lin H, et al., Natl. Sci. Rev. 9 (2022) nwac022.
[10] Q. Chen, Y. Liu, Y. Lu, et al., J. Hazard. Mater. 422 (2022) 126929.
[11] G. Fang, R. Kang, S. Cai, C. Ge, Nano Today 48 (2023) 101755.
[12] M. Chan, B. Chen, W. Huang, et al., Mater. Today Adv. 17 (2023) 100342.
[13] S. Li, Y. Hou, Q. Chen, et al., ACS Appl. Mater. Interfaces 12 (2020) 2581–2590.
[14] J. Sheng, Y. Wu, H. Ding, et al., Adv. Mater. 36 (2024) 2211210.
[15] Q. Wang, C. Li, X. Wang, et al., Nano Lett. 22 (2022) 10003–10009.
[16] L. Zuo, H. King, M.A. Hossain, et al., Chem. Biomed. Imaging 1 (2023) 760–766.
[17] Y. Kang, C. Li, H. Shi, et al., Chin. J. Chem. 41 (2023) 3189–3196.
[18] W. Gao, J. He, L. Chen, et al., Nat. Commun. 14 (2023) 160.
[19] Y. Sun, B. Xu, X. Pan, et al., Coord. Chem. Rev. 475 (2023) 214896.
[20] G. Wei, S. Liu, Y. Peng, H. Wei, Chin. J. Chem. 42 (2024) 1515–1522.
[21] B. Zhang, J. Zhang, F. Zhang, et al., Adv. Funct. Mater. 30 (2020) 1906194.
[22] M.A. Ghausi, J. Xie, Q. Li, et al., Angew. Chem. Int. Ed. 57 (2018) 13135–13139.
[23] Z. Chen, X. Su, J. Ding, et al., Appl. Catal. B 308 (2022) 121206.
[24] T. Li, H. Xu, Cell Rep. Phys. Sci. 1 (2020) 100111.
[25] F. Qiao, J. Wang, S. Ai, L. Li, Sens. Actuators B 216 (2015) 418–427.
[26] Q. Wang, T. Ina, W. Chen, et al., Sci. Bull. 65 (2020) 1743–1751.
[27] Y. Zhong, B. Li, S. Li, et al., Nano-Micro Lett. 10 (2018) 56.
[28] Z.M.S.H. Khan, S.A. Khan, M. Zulfequar, Mater. Sci. Semicond. Process. 57 (2017) 190–196.
[29] W. Qu, F. Shen, H. Zu, et al., Energy Fuels 34 (2020) 9779–9786.
[30] A. Nezhadali, L. Mehri, R. Shadmehri, Mater. Sci. Eng. C 85 (2018) 225–232.
[31] F. Lega, L. Contiero, G. Biancotto, R. Angeletti, Food Addit. Contam. A 30 (2013) 949–957.
[32] K. Kusmierek, E. Bald, Talanta 71 (2007) 2121–2125.
[33] C. Yu, D. Qin, X. Jiang, X. Zheng, B. Deng, Microchem. J. 168 (2021) 106480.
[34] A. Kutluay, M. Aslanoglu, Sens. Actuators B 171–172 (2012) 1216–1221.
[35] H. Lai, G. Li, Z. Zhang, Sens. Actuators B 380 (2023) 133325.
[36] X. Liao, Y. Chen, M. Qin, et al., Talanta 117 (2013) 203–208.
[37] G.M. Fernandes, W.R. Silva, D.N. Barreto, et al., Anal. Chim. Acta 1135 (2020) 187–203.
[38] M. Feng, X. Li, X. Zhang, Y. Huang, Trends Anal. Chem. 166 (2023) 117220.
[39] Z. Wang, X. Jin, C. Zhu, et al., Adv. Mater. 33 (2021) 2104718.
[40] L. Jiao, W. Xu, Y. Zhang, et al., Nano Today 35 (2020) 100971.
[41] J. Xu, Q. Liang, Z. Li, et al., Adv. Mater. 34 (2022) 2200011.
[42] B. Yang, S. Liu, Y.V. Fedoseeva, et al., J. Power Sourc. 493 (2021) 229700.
[43] K. Zhang, X. Min, T. Zhang, et al., J. Hazard. Mater. 413 (2021) 125294.
[44] Z. Qiao, L. Lin, X. Yan, et al., Chem. Asian J. 15 (2020) 3620–3636.
[45] C. Chen, L. Zhou, H. Zhang, et al., ACS EST Eng. 3 (2023) 248–259.
[46] S. Liu, Q. Pan, J. Li, et al., ACS EST Water 2 (2022) 817–829.
[47] H. Hu, J. Wang, B. Cui, et al., Angew. Chem. Int. Ed. 61 (2022) e202114441.
[48] M. Wang, Z. Sun, H. Ci, et al., Angew. Chem. Int. Ed. 60 (2021) 24558–24565.
[49] W. Ni, Z. Liu, Y. Zhang, et al., Adv. Mater. 33 (2020) 2003238.
[50] Q. Wu, Y. Jia, Q. Liu, et al., Chem 8 (2022) 1–19.
[51] X. Guo, H. Zhang, Y. Yao, et al., Appl. Catal. B 323 (2023) 122136.
[52] A.M. Chaparro, C. Maffiotte, Surf. Sci. Spectra 8 (2001) 105–116.
[53] L. Jiao, J. Wu, H. Zhong, et al., ACS Catal. 10 (2020) 6422–6429.
[54] S. Dong, Y. Dong, B. Liu, et al., Adv. Mater. 34 (2022) 2107054.
[55] J. Xiao, X. Yang, X. Zhao, et al., Biochem. Eng. J. 202 (2024) 109165.
[56] Y. Zhu, W. Wang, J. Cheng, et al., Angew. Chem. Int. Ed. 60 (2021) 9480–9488.
[57] M. Ma, H. Wang, T. Zhang, et al., ACS Omega 8 (2023) 35779–35790.
[58] C. Zhang, C. Chen, D. Zhao, et al., Anal. Chem. 94 (2022) 3485–3493.
[59] Y. Huang, Z. Ding, Y. Li, F. Xi, J. Liu, Molecules 28 (2023) 4573.
[60] A.M. Ariti, S.A. Geleto, B.T. Gutema, et al., Sens. Bio-Sen. Res. 42 (2023) 100595.
[61] H. Liu, Z. Gao, H. Yan, et al., Sci. China Chem. 66 (2023) 2590–2599.
[62] P. Li, Y. Feng, D. Cheng, J. Wei, J. Colloid Interface Sci. 625 (2022) 435–445.
[63] S. Wang, Z. Li, M. Xia, et al., Chem. Res. Chin. Univ. 6 (2023) 907–914.
[64] Z. Wang, J. Liu, M. Feng, et al., Chem. Eng. J. 470 (2023) 144020.
[65] H. Wang, W. Bao, M.T. Sarwar, et al., Inorg. Chem. 62 (2023) 8418–8427.
[66] Y. Ma, M. Zhang, J. Wu, et al., Small 19 (2023) 2300883.
[67] L. Gao, J. Zhuang, L. Nie, et al., Nat. Nanotechnol. 2 (2007) 577–583.
[68] Y. Wang, T. Li, H. Wei, Anal. Chem. 95 (2023) 10105–10109.
[69] X. Li, H. Zhu, P. Liu, et al., Trends Anal. Chem. 143 (2021) 116379.
[70] S. Lin, Y. Zhang, W. Cao, et al., Dalton Trans. 48 (2019) 1993–1999.